Electronic Supplementary Information (ESI)

3D periodic polyimide nano-networks for ultrahigh-rate and sustainable energy storage

Youngjin Ham,[a] Nathan J. Fritz,[b] Gayea Hyun,[a] Young Bum Lee,[b] Jong Seok Nam,[a] Il-Doo Kim,*[a] Paul V. Braun,*[bc] and Seokwoo Jeon*[ad]

[a] Department of *Materials Science and Engineering, Korea Advanced Institute of Science and Technology (KAIST), 291 Daehak-ro, Yuseong-gu, Daejeon 34141, Republic of Korea.*

[b] *Department of Materials Science and Engineering, University of Illinois Urbana-Champaign, Urbana, Illinois 61801, USA.*

[c] *Materials Research Laboratory and Beckman Institute for Advanced Science and Technology, University of Illinois Urbana-Champaign, Urbana, Illinois 61801, USA.*

[d] *Advanced Battery Center, KAIST Institute for the NanoCentury, 291 Daehak-ro, Yuseong-gu, Daejeon 34141, Republic of Korea.*

Supplementary Text

XPS analysis of the as-fabricated 3D PIN/Ni in Fig. S5: The chemical composition of the as-fabricated 3D PIN/Ni was identified by X-ray photoelectron spectroscopy (XPS) analysis. In Fig. S5, the Ni 2p spectra revealed four peaks corresponding to the Ni $2p_{1/2}$, Ni $2p_{3/2}$, and their satellites, indicating the surface oxidation of the 3D Ni during the removal of the epoxy template.[1] The four de-convoluted regions in the C 1s spectra could be assigned to the sp2 carbon (284.7 eV), C−C/C−H (285.2 eV), C−N/C−O (286.1 eV), and C=O (288.8 eV) groups, respectively. Similarly, the O 1s core-level could be divided into peaks located at 532.2, 533.0, and 533.8 eV, which we attribute to C=O, O=C−OH, and C−O bonding. For N 1s spectra, two peaks with the binding energies of 399.5 and 400.5 eV were assigned to the amide and aromatic imide which can provide the key redox-active centers. Taken together, the XPS data confirms the successful formation of the PIN layer on the 3D Ni, being consistent with the proposed molecular structure of the PIN in Fig. 1b.

Li^+ diffusion coefficient (D_{Li}) calculation by the Warburg factor associated with Z': D_{Li} can be derived according to the following equation:[2]

$$D_{Li} = \frac{R^2T^2}{2A^2n^4F^4c^2\sigma^2} \quad (1)$$

where R represents the gas constant, T is the absolute temperature, A stands for the electrode surface area, n is the number of transferred electrons, F is Faraday's constant, and c is the molar concentration of Li^+. σ corresponds to the Warburg factor associated with Z´ in the low-frequency region, as follows:[2]

$$Z' = R_b + R_{ct} + \sigma\omega^{-1/2} \quad (2)$$

where R_b and ω are ohmic resistance and angular frequency, respectively.

TEM analysis of 3D PIN/Ni-4 and 3D PIN/Ni-40 in Fig. S9: While the TEM image of the 3D PIN/Ni-10 showed that the few-layered PIN particles are homogeneously formed on the 3D Ni, the density of the PIN particles (mass loading = 24.1 wt%) in the 3D PIN/Ni-4 is not high enough to cover the whole Ni surfaces and only the upper surface of each particle is expected to be exposed to the electrolyte. The much lower electrolyte contact area of single-layered PIN particles compared to that of few-layered PIN particles in 3D PIN/Ni-10 leads to the limited formation of the SEI layer, reducing the number of lithium ions consumed by the SEI formation, thus contributing to smaller initial irreversible capacity.[3] Our evidence for this is the large difference in the first-cycle capacity (i.e., initial CE) of the 3D PIN/Ni-4 compared with the other two electrodes, which are discussed more with EIS results in Fig. S12.

In the 3D PIN/Ni-40, the highest PIN mass loading of 55.6 wt% on the Ni surface results in aggregation, where the coated PIN particles appear as dark spots, explaining the rapid capacity degradation of 3D PIN/Ni-40 in Fig. 1g.

Capacitive and diffusion-controlled contributions: As the peak current (i) at the certain scan rate (ν) follows the power law: $i = av^b$, the b values which reflect the lithium storage behaviors can be calculated from the plots of log(i) versus log(ν). Specifically, the b value of 0.5 implies that the electrode undergoes a pure faradaic process limited by ion diffusion, and the b value of 1.0 indicates a capacitive process where the storage mechanism is a surface phenomenon.[4]

Quantitatively, the capacitive and diffusion-controlled contributions on the overall capacity are differentiated, using the following expression:[5]

$$i = k_1\nu + k_2\nu^{1/2} \quad (3)$$

Energy density targets of virtual cells in Fig. 5b: The required specific and volumetric capacities of anode materials in Fig. 5b can be calculated as follows:[6]

$$C_{\text{specific. or vol.}} = \frac{E_{\text{specific. or vol. target}}}{U_C - U_A} \quad (4)$$

Where U_C represents the average cathode voltage and U_A stands for the average anode voltage. The target lines for specific and volumetric capacities are consistent for each cathode class. Used U_C values for the conversion (e.g., FeF_3), layered intercalation (e.g., Ni-rich NMC), high-voltage spinel cathodes (e.g., $LiNi_{0.5}Mn_{1.5}O_4$), and p-type organic cathodes (e.g., 5,10-dihydro-5,10-dimethylphenazine [7]) were 2.0, 3.8, 4.7, and 3.6 V, respectively. We used the energy targets (125 Wh kg^{-1} at battery pack level) of hybrid electric vehicles which is anticipated for 2025.[6]

Supporting Figures

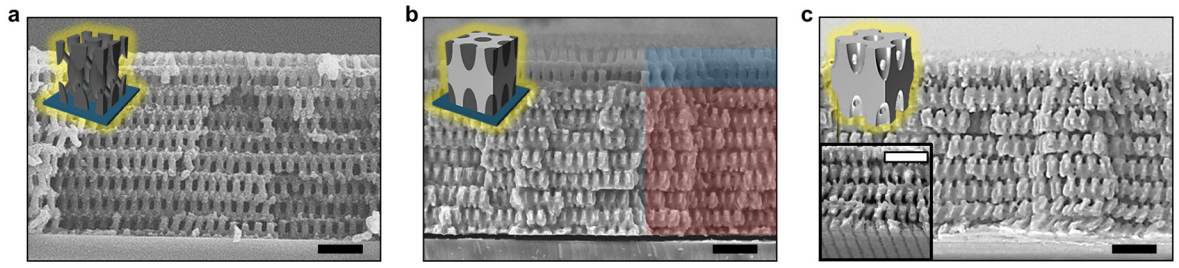

Fig. S1 Cross-sectional view SEM images of a) 3D epoxy template, b) epoxy template with electroplated Ni, and c) free-standing 3D Ni (scale bars, 2 μm) with schematic illustrations. The colorized right side in (b) highlights each structure (red: epoxy with electroplated Ni; blue: epoxy).

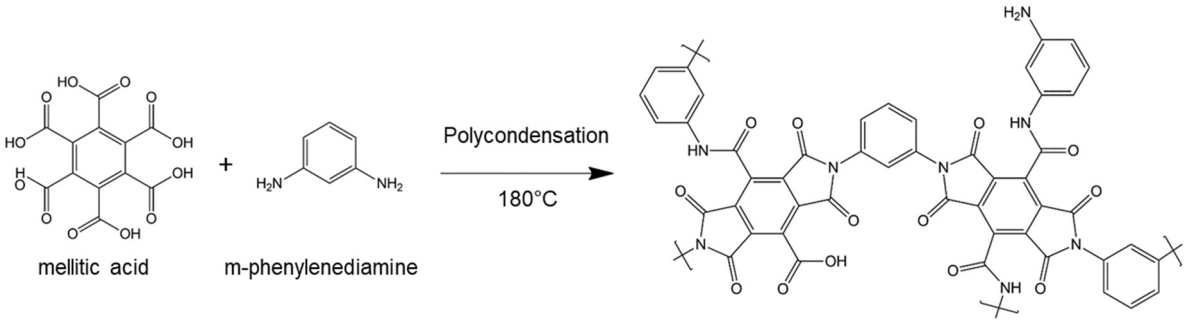

Fig. S2 Polycondensation reaction of mellitic acid and m-phenylenediamine. The reaction product is the expected unit molecular structure of PIN.

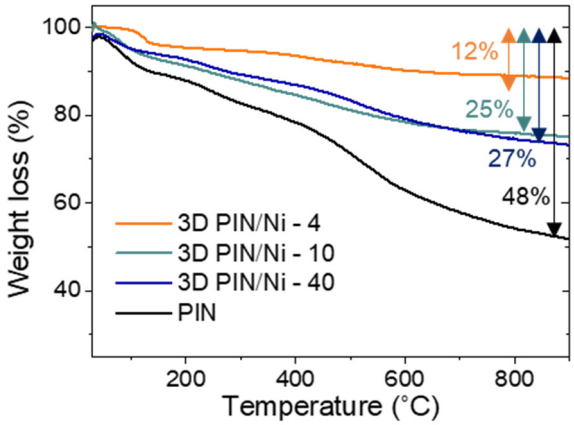

Fig. S3 Thermogravimetric analysis of the 3D PIN/Ni electrodes prepared with different concentrations of the precursor solution. The mass loading of the redox-active PIN was controlled by varying the concentration of the precursor solutions (4, 10, and 40 mg mL^{-1}). We term these anodes prepared with 4, 10, and 40 mg mL^{-1} of precursor solutions 3D PIN/Ni-4, 3D PIN/Ni-10, and 3D PIN/Ni-40, respectively. The continuous weight loss of the 3D PIN/Ni in the range of 30 to 900 °C accounts for the decomposition of PIN (48% loss) in the electrodes. The mass loadings of PIN in the 3D PIN/Ni-4, -10, and -40 electrodes are estimated to be 24.1, 51.7, and 55.6 wt%, respectively.

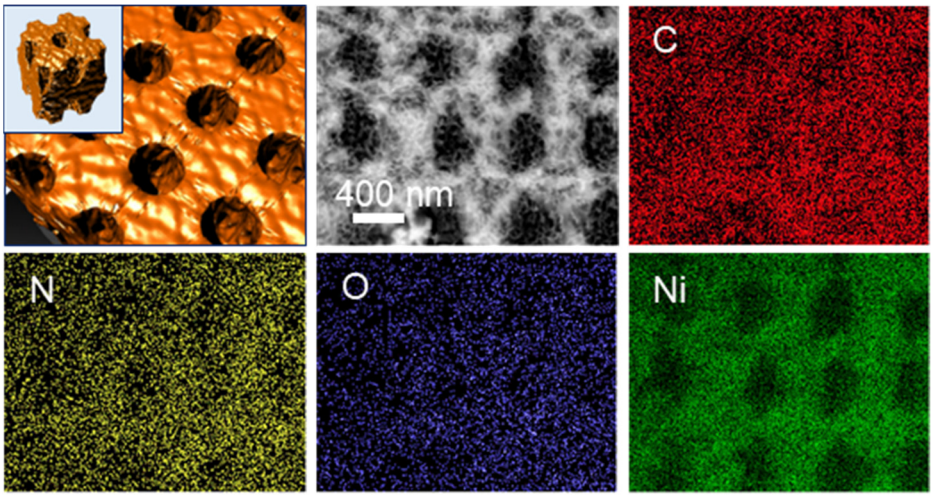

Fig. S4 In-situ elemental mapping results of the 3D PIN/Ni analyzed by energy-dispersive X-ray spectroscopy.

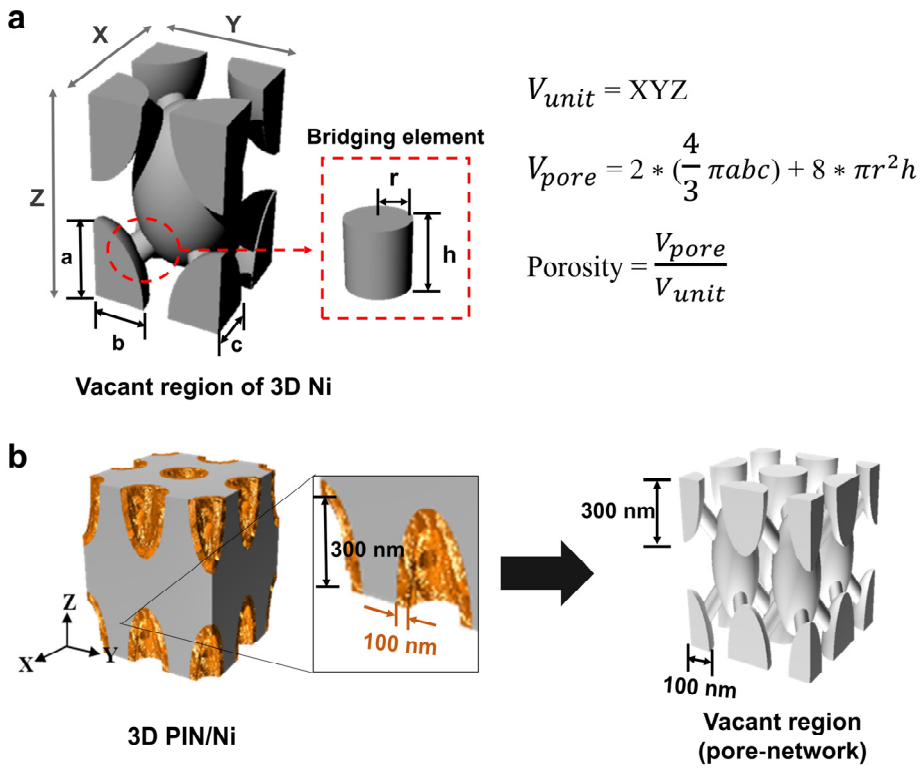

Fig. S5 Schematic images of unit structure prepared by PnP technique with detailed parameters for the calculation of porosity. a) The vacant region of 3D Ni scaffold. The unit cell consists of ellipsoids (prolate spheroid) and each ellipsoid is interconnected through bridging elements in a cylindrical shape (radius r, height h). Parameters for the unit cell with periodicity of 600 nm: X = Y = 0.6, Z =1, a = 0.4, b = c = 0.2, r = 0.15, h= 0.15. b) 3D PIN/Ni and its vacant region, which will be filled with electrolyte. Parameters for the unit cell of vacant region: a = 0.3, b = c = 0.1, r = 0.05, h= 0.35. The geometrically calculated porosity of the 3D PIN/Ni is estimated to be in the range of 13 to 30%.

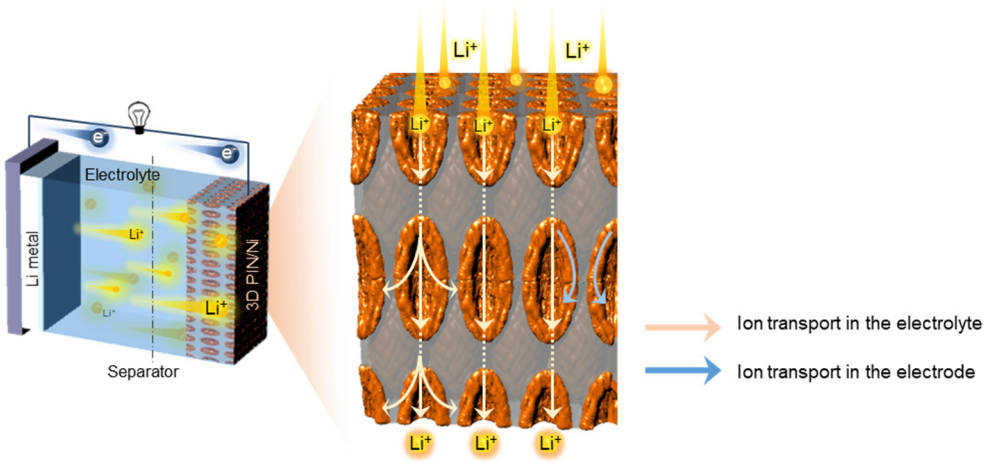

Fig. S6 Schematic illustration depicting rapid ion transport in the 3D PIN/Ni. The short solid-phase diffusion length through the nano-sized PIN layer minimizes the effect of sluggish solid-state transport of ions within the electrode. Furthermore, the low-tortuosity structural design of the 3D PIN/Ni enables rapid ion transport in the electrolyte through the well-ordered porous network.

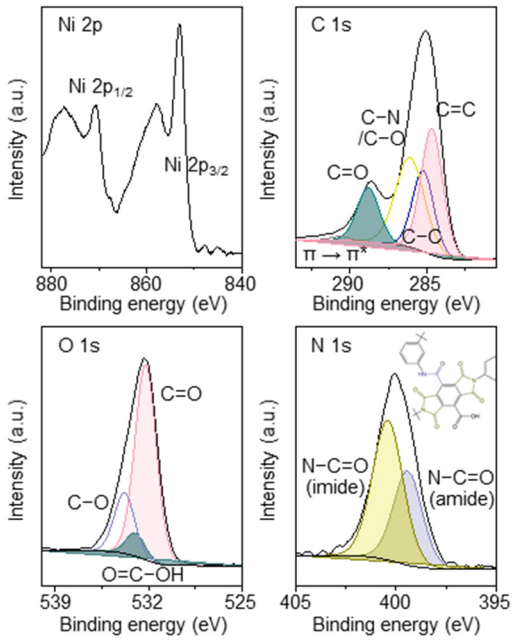

Fig. S7 XPS spectra of the as-fabricated 3D PIN/Ni.

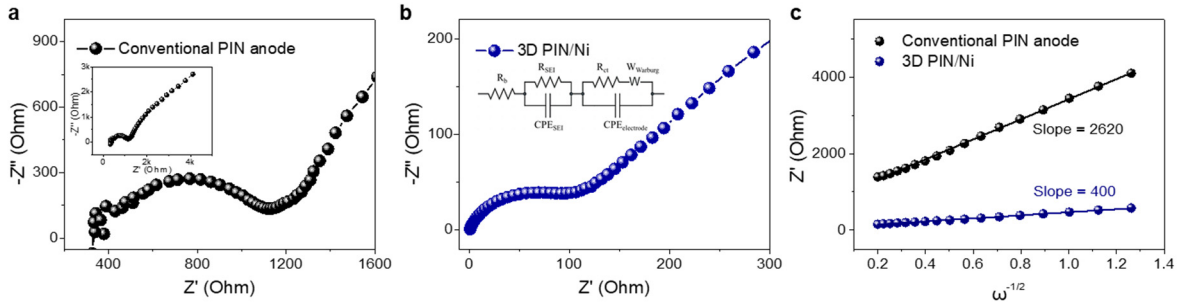

Fig. S8 EIS profiles and analysis of ion diffusion. The Nyquist plots of a) the conventional PIN anode and b) the 3D PIN/Ni at the fully charged state after 2 cycles. c) The relationships between Z′ and $\omega^{-1/2}$ in the Warburg region derived from (a) and (b). The slope of the fitted line corresponds to the Warburg factor.

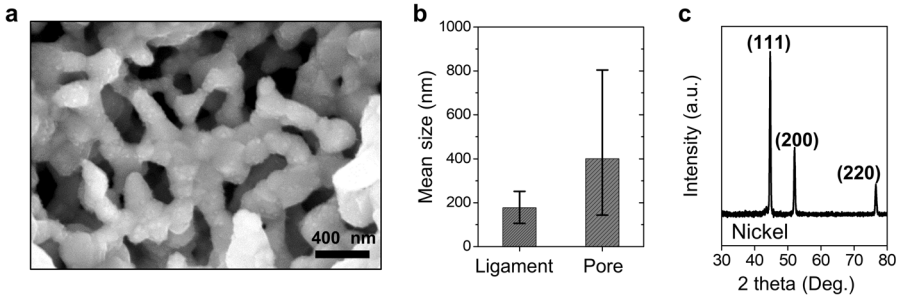

Fig. S9 Synthesis of the random porous Ni foam using the reported method of hydrogen thermal reduction of nickel nitrate hexahydrates at 450 °C. [8] a) SEM image, b) Mean size of ligament and pores, and c) XRD pattern of the synthesized random porous Ni foam. All of the diffraction peaks are corresponding to pure Ni (standard card JCPDS 04-0850).

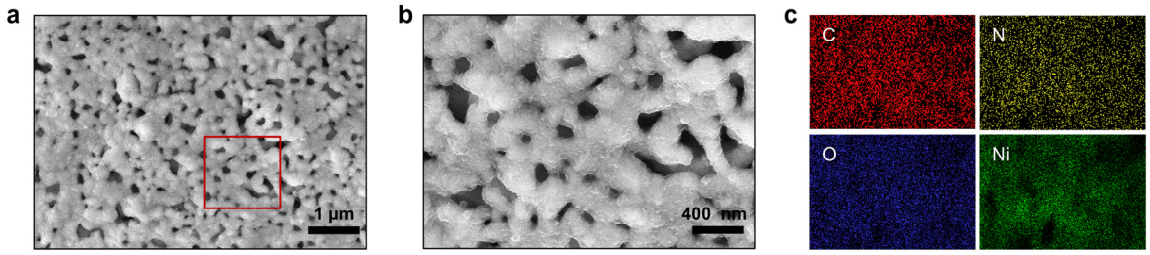

Fig. S10 a) Low- and b) high-magnification SEM images of the PIN/Ni foam. c) In-situ elemental mapping results of the PIN/Ni foam.

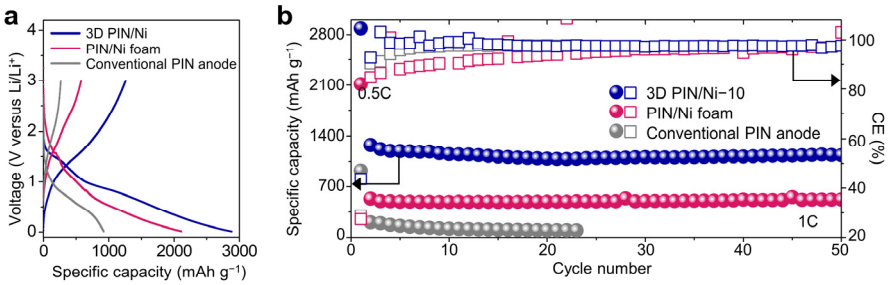

Fig. S11 a) Initial galvanostatic lithiation/delithiation profiles of the 3D PIN/Ni, the random porous PIN/Ni foam, and the conventional PIN anode for the first electrochemical cycle within a voltage range of 0.01−3 V at 0.5C rate. b) Cycling performance and CE.

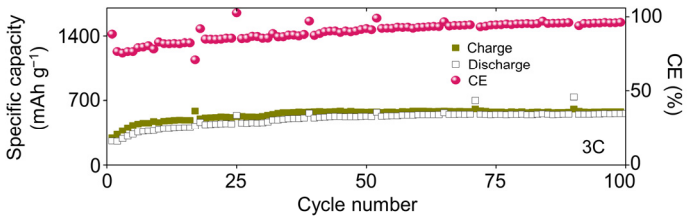

Fig. S12 Cycling performance and CE of the PIN/Ni foam over 100 cycles at 3C rate.

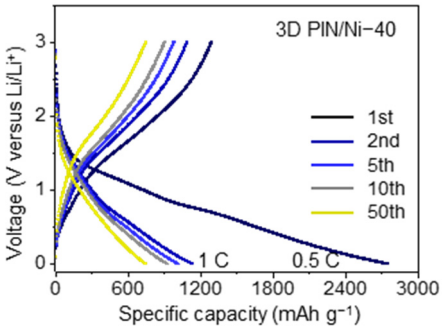

Fig. S13 Galvanostatic lithiation/delithiation profiles of the 3D PIN/Ni-40 over 50 cycles.

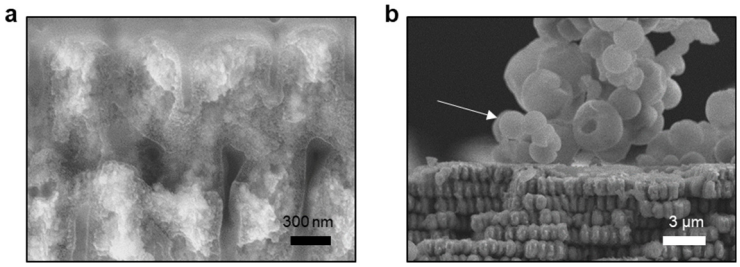

Fig. S14 SEM images of the 3D PIN/Ni prepared with precursor solutions above the critical concentration. a) Cross-sectional SEM image of the 3D PIN/Ni-40. b) SEM image of the 3D PIN/Ni-20 showing the growth of microparticle impurities on the top surface. The impurities are likely crystalline precipitates formed by a high concentration of precursor solutions (>20 mg mL^{-1}).

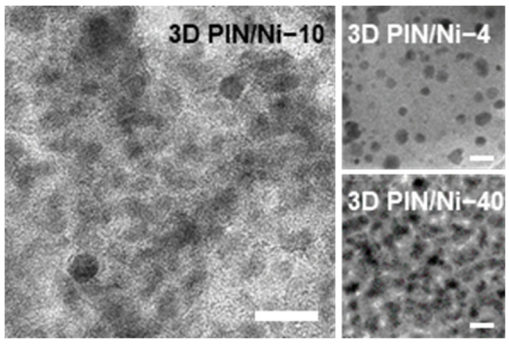

Fig. S15 Representative TEM images of the 3D PIN/Ni-4, -10, and -40 (scale bars, 20 nm).

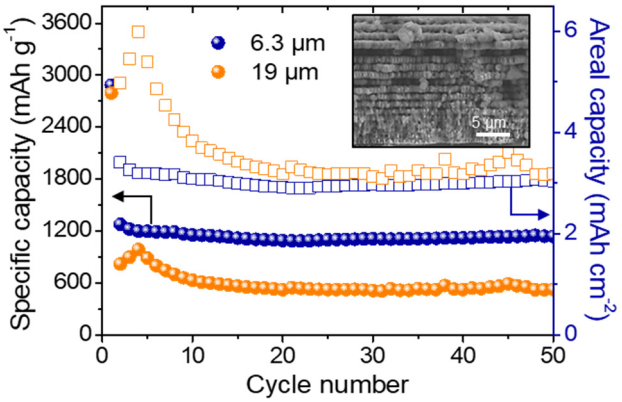

Fig. S16 Specific and areal capacities of the 3D PIN/Ni-10 with thicknesses of 6. 3 and 19 μm over 50 cycles. Active mass loading densities are 2.7 and 6.1 mg cm^{-2} for 6. 3 and 19 μm-thick electrodes, respectively.

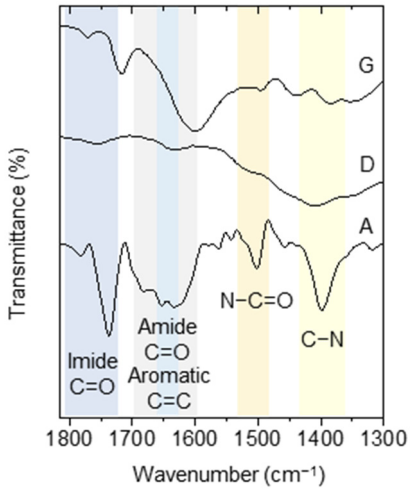

Fig. S17 FT-IR spectra of the 3D PIN/Ni at the different electrochemical states; as-prepared (point A), fully-lithiated (point D), and delithiated (point G) states. The as-prepared 3D PIN/Ni shows characteristic peaks related to C=O in imide (1784 and 1737 cm^{-1}), C=O in amide (1656 cm^{-1}), aromatic C=C bonds in benzene rings (1633 cm^{-1}), N−C=O (1502 cm^{-1}), and C−N bonds (1398 cm^{-1}). The most notable change in the FT-IR spectrum could be found in the region of 1600−1800 cm^{-1} where the stretching of C=O and C=C bonds disappear with discharging and reversibly recover at the delithiated state. The peak broadening at fully-lithiated state is attributed to the overlapped C=O stretching modes of Li_2CO_3 indicative of the formation of the SEI layer, which is consistent with the XPS data and the previous reports.[9]

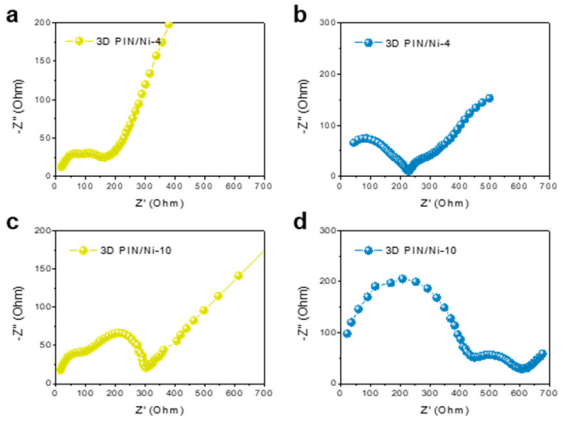

Fig. S18 The Nyquist plots during SEI formation. The 3D PIN/Ni-4 at the a) C state and b) D state. The 3D PIN/Ni-10 at the c) C state and d) D state.

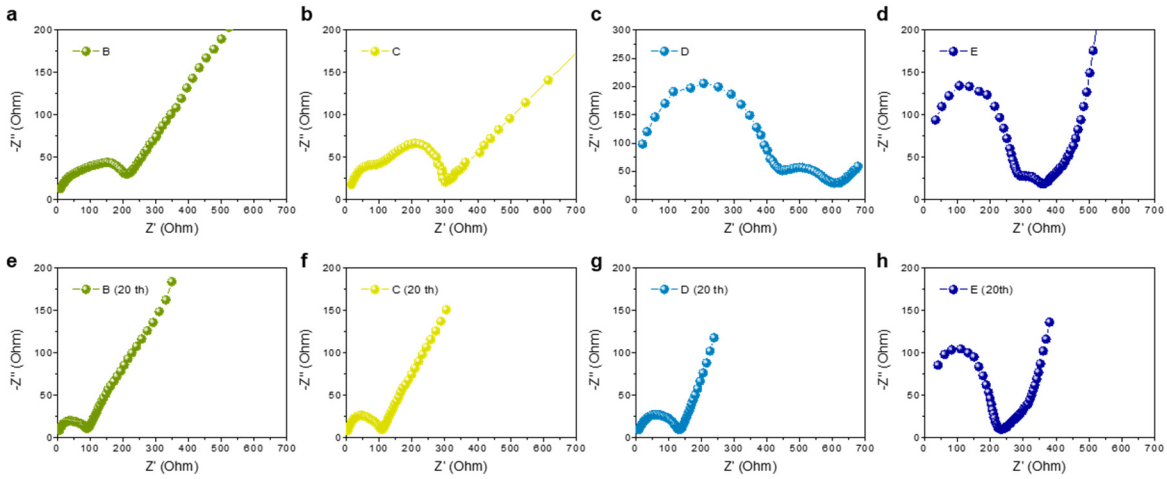

Fig. S19 The Nyquist plots of the 3D PIN/Ni at different SOCs and DODs. a−d) In the 1st cycle. e−h) In the 20th cycle.

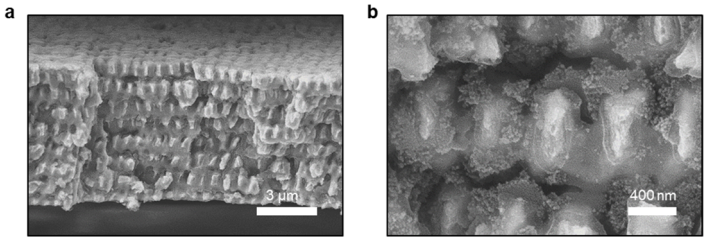

Fig. S20 SEM images of the 3D PIN/Ni after 250 cycles at 10C rate.

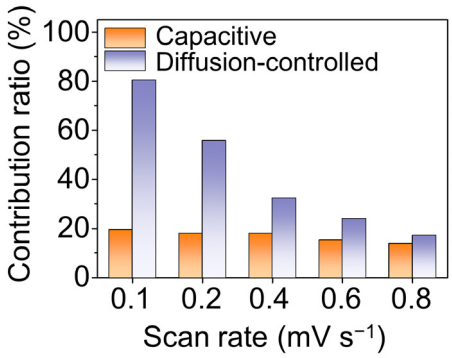

Fig. S21 The contribution ratio of capacitive and diffusion-controlled capacities reflecting real total capacity at each scan rate, calculated by taking total capacity at 0.1 mV s^{-1} as 100%.

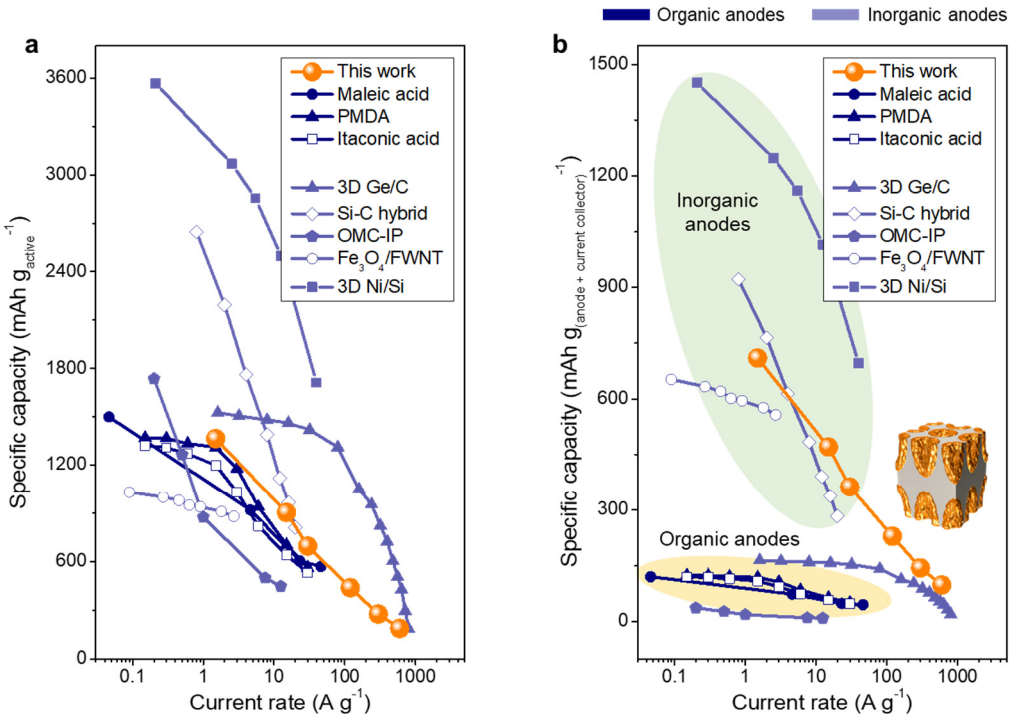

Fig. S22 Comparison of rate capability of the 3D PIN/Ni with various organic and inorganic anode materials reported for high-performance LIBs. Those materials include silicon-based anode with a high theoretical capacity of 4200 mAh g^{-1}. a) Specific capacity based on the mass of active materials. b) The calculated capacity based on the total weight of the anode components including active materials, conducting additive, binder, and the current collector, if applicable.

Supporting Tables

Table S1. List of EIS fitting parameters and the Warburg factor of the conventional PIN anode and the 3D PIN/Ni at the fully charged state after 2 cycles.

	R_b (Ω)	R_{SEI} (Ω)	R_{ct} (Ω)	σ
conventional PIN anode	355	92.0	559	2620
3D PIN/Ni	1.30	9.20	71.9	400

Table S2. Peak assignments for XPS spectra of C 1s and N 1s regions for the 3D PIN/Ni at the different electrochemical states in the first cycle.

Bonds		Binding energy (eV)				
		A state	B state	C state	D state	G state
C 1s	C=C	284.7	284.7	283.7	-	284.9
	C−C/C−H	285.2	285.3	284.9	285.2	285.3
	C−N/C−O	286.1	286.1	286.1	286.3	286.1
	C−OLi	-	-	287.6	287.1	-
	C=O	288.8 (COOH)	288.4 (COOLi)	288.8 (weak)	-	288.4 (COOLi)
	C−Li	-	-	-	290.3	289.9 (weak)
	Pi-pi*	290.6	290.4	290.4	-	290.5
O 1s	C=O	532.2	532.1	-	-	532.1
	O=C−OH	533.0	-	-	-	-
	C−O	533.8	533.7	533.0	532.2	533.6
	O−Li	-	531.3	531.5	531.3	531.0
	R−O−Li (SEI film)	-	-	530.1	530.6	-

Table S3. List of EIS fitting parameters of the 3D PIN/Ni at the different electrochemical states in the first cycle.

	R_b (Ω)	R_{SEI} (Ω)	R_{ct} (Ω)
B	11.2	62.2	127
C	16.8	89.3	177
D	0.700	426	154
E	1.70	279	81.7
F	10.8	46.6	185
G	1.40	12.5	90.9

Table S4. Comparison of EIS fitting parameters of the 3D PIN/Ni-4 and -10 during SEI formation.

State	Electrode	R_b (Ω)	R_{SEI} (Ω)	R_{ct} (Ω)
C	3D PIN/Ni-4	15.9	53.2	88.3
	3D PIN/Ni-10	16.8	89.3	177
D	3D PIN/Ni-4	13.4	152	58.8
	3D PIN/Ni-10	0.700	426	154

Table S5 Summary of electrode composition of organic-based anodes in Fig. 5a.

Material	Electrode composition	Current collector
3D PIN/Ni	PIN:Ni = 52:48	X (free-standing)
Maleic acid	Active:acetylene black:binder = 50:40:10	Cu
IBN/SWCNT	Active:SWCNT = 80:20	X
1,4,5,8-naphthalenetetracarboxylic dianhydride (NTCDA)	Active:diatomite+super P:binder = 42:48:10	Cu
Poly(benzobisimidazobenzo-phenanthroline) (BBL)	Active:CNT:binder = 70:20:10	Cu
Itaconic acid	Active:acetylene black:binder = 50:40:10	Cu
Tetrahydroxybenzoquinone/ graphene oxide (THBQ/GO)	Active:GO:super P:binder = 35:35:15:15	Cu
Maleic acid/G	Active:graphite:acetylene black:binder=30:30:30:10	Cu
Pyromellitic dianhydride (PMDA)	Active:acetylene black:cellulose:copolymers = 50:40:5:5	Cu
Nickel 2,6-naphthalenedicarboxylate with single-walled CNT (NiNDC/SWCNT)	Active(metal-organic):SWCNT:polyacrylonitrile = 70:7:23	X

Table S6. Performance of reported anode materials for LIBs.

Material	Electrode composition	Specific capacity (mAh g_{active}^{-1})	Capacity per total weight (mAh $g_{(anode + current\ collector)}^{-1}$) [a)]	Maximum areal capacity (mAh cm^{-2})	Reference
Organic based anode					
3D PIN/Ni	PIN:Ni = 52:48	1277	664.0	5.99	This work
Maleic acid	Active:acetylene black:binder = 50:40:10	1500	120.3	0.525	[10]
PMDA	Active:acetylene black:cellulose:copolymers = 50:40:5:5	1535	139.1	0.614	[11]
Itaconic acid	Active:acetylene black:binder = 50:40:10	1270	109.4	0.530	[12]
Inorganic based anode					
3D Ge/C	Active:Super P:lithium polyacrylate = 80:10:10	~1604	172.9	2.97	[13]
Si-C hybrid	Active:Super P:binder = 80:10:10	2646	922.4	~6.00	[14]
Ordered mesoporous carbon with interconnected pore (OMC-IP)	Active:Super P:binder = 80:10:10	2201	37.30	0.195	[15]
Spherical Fe_3O_4/carbon black/few-walled CNT web electrode (Fe_3O_4/FWNT)	Active (Fe_3O_4) = 63.3 wt%, without Cu current collector	1031	652.6	2.30	[16]
3D Ni supported bicontinuous Si (3D Ni/Si)	Si:Ni = 41:59, without Cu current collector	3568	1450	-	[17]

[a)]Capacity per total weight of the anode components including active materials, conducting additive, binder, and current collector

References

[1] S. Kim, C. Ahn, Y. Cho, G. Hyun, S. Jeon and J. H. Park, *Nano Energy*, 2018, **54**, 184−191.

[2] C. Li, S. Dong, R. Tang, X. Ge, Z. Zhang, C. Wang, Y. Lu and L. Yin, *Energy Environ. Sci.*, 2018, **11**, 3201−3211.

[3] F. Zhang, G. Zhu, K. Wang, X. Qian, Y. Zhao, W. Luo and J. Yang, *J. Mater. Chem. A*, 2019, **7**, 17426−17434.

[4] V. Augustyn, J. Come, M. A. Lowe, J. W. Kim, P.-L. Taberna, S. H. Tolbert, H. D. Abruña, P. Simon and B. Dunn, *Nat. Mater.*, 2013, **12**, 518−522.

[5] S. Zheng, H. Huang, Y. Dong, S. Wang, F. Zhou, J. Qin, C. Sun, Y. Yu, Z.-S. Wu and X. Bao, *Energy Environ. Sci.*, 2020, **13**, 821−829.

[6] D. Andre, H. Hain, P. Lamp, F. Maglia and B. Stiaszny, *J. Mater. Chem. A,* 2017, **5,** 17174−17198.

[7] Y. Ham, V. Ri, J. Kim, Y. Yoon, J. Lee, K. Kang, K.-S. An, C. Kim and S. Jeon, *Nano Res.*, 2021, **14**, 1382−1389.

[8] L. Lu, P. Andela, J. T. M. De Hosson and Y. Pei, *Appl. Nano Mater.*, 2018, **1**, 2206−2218.

[9] J. Ryu, B. Park, J. Kang, D. Hong, S.-D. Kim, J.-K. Yoo, J. W. Yi, S. Park and Y. Oh, *ACS Nano*, 2019, **13**, 14357−14367.

[10] Y. Wang, Y. Deng, Q. Qu, X. Zheng, J. Zhang, G. Liu, V. S. Battaglia and H. Zheng, *ACS Energy Lett.*, 2017, **2**, 2140−2148.

[11] R. Guo, Y. Wang, S. Heng, G. Zhu, V. S. Battaglia and H. Zheng, *J. Power Sources*, 2019, **436**, 226848.

[12] Y. Wang, W. Liu, R. Guo, Q. Qu, H. Zheng, J. Zhang and Y. Huang, *J. Mater. Chem. A*, 2019, **7**, 22621−22630.

[13] D. T. Ngo, H. T. Le, C. Kim, J.-Y. Lee, J. G. Fisher, I.-D. Kim and C.-J. Park, *Energy Environ. Sci.*, 2015, **8**, 3577−3588.

[14] X. Zhang, D. Wang, X. Qiu, Y. Ma, D. Kong, K. Müllen, X. Li and L. Zhi, *Nat. Commun.*, 2020, **11**, 1−9.

[15] Y. Liang, L. Chen, L. Cai, H. Liu, R. Fu, M. Zhang and D. Wu, *Chem. Commun.*, 2016, **52**, 803−806.

[16] Y. H. Kwon, J. J. Park, L. M. Housel, K. Minnici, G. Zhang, S. R. Lee, S. W. Lee, Z. Chen, S. Noda and E. S. Takeuchi, *ACS Nano*, 2018, **12**, 3126−3139.

[17] H. Zhang and P. V. Braun, *Nano Lett.*, 2012, **12**, 2778−2783.